ELSEVIER

Chemical Geology 240 (2007) 36–53

CHEMICAL GEOLOGY
INCLUDING
ISOTOPE GEOSCIENCE

www.elsevier.com/locate/chemgeo

Heterogeneous mantle argon isotope composition in the subcontinental lithospheric mantle beneath the Red Sea region

Jens Hopp [a,*], Mario Trieloff [a], Alexei I. Buikin [a,b], Ekaterina V. Korochantseva [a,b], Winfried H. Schwarz [a], Tilmann Althaus [c], Rainer Altherr [a]

[a] *Mineralogisches Institut der Universität Heidelberg, Im Neuenheimer Feld 236, D-69120 Heidelberg, Germany*
[b] *Vernadsky Institute for Geochemistry, Kosygin St. 19, 117975 Moscow, Russia*
[c] *Max-Planck Institut für Astronomie, Redaktion Sterne und Weltraum, Königstuhl 1, D-69117 Heidelberg, Germany*

Received 22 November 2005; received in revised form 27 November 2006; accepted 8 January 2007

Editor: S.L. Goldstein

Abstract

We performed argon measurements on rocks of the subcontinental lithospheric mantle (SCLM) from the Red Sea region applying stepwise crushing extractions, and argon analyses using high-resolution stepwise heating techniques, the latter combined with $^{40}Ar/^{39}Ar$ dating. Maximum $^{40}Ar/^{36}Ar$ ratios of individual samples range from 4190±240 to 25,590±620, the latter (sample SA 87-2/12) being the highest measured value of any mantle peridotite or pyroxenite sample so far. For five samples, reasonably defined binary mixing correlations between atmospheric and mantle-derived argon and neon resulted in calculated sample-specific mantle-$^{40}Ar/^{36}Ar$ ratios of 5040±50, 7500±70, 9510±220, 29,600±2700, and 39,000±2500 at an assumed mantle-$^{20}Ne/^{22}Ne$ value of 12.5. These observations indicate a highly heterogeneous argon isotopic composition of the trapped mantle fluids. Furthermore, most samples exhibit mantle-$^{36}Ar/^{22}Ne$ ratios higher than considered to represent an unfractionated mantle source. These characteristics could be explained by mixing of plume-related (low $^{40}Ar/^{36}Ar$) and lithospheric (high $^{40}Ar/^{36}Ar$) melts or fluids following elemental fractionation between Ar and Ne. Alternatively, we propose the presence of a severely fractionated atmospheric component highly enriched in argon, admixed to the mantle fluids before trapped by the ultramafic rocks. This primary, seriously fractionated atmospheric component cannot be monitored by Ne isotopes. Incorporation of such a primary atmospheric component could occur either during magma ascent at relatively shallow, upper crustal levels, or by mobilization of atmospheric fluids in a subduction-related metasomatized lithospheric mantle during Pan African times (c. 600–800 Ma ago).

Keywords: Argon isotopes; Subcontinental lithospheric mantle; Red Sea; Atmospheric fluids

1. Introduction

Variations in argon isotopes in different mantle domains are dominated by different time-integrated accumulation of radiogenic $^{40}Ar^*$ from ^{40}K decay.

* Corresponding author. Tel.: +49 6221 544895; fax: +49 6221 544805.
E-mail address: jhopp@min.uni-heidelberg.de (J. Hopp).

0009-2541/$ - see front matter © 2007 Elsevier B.V. All rights reserved.
doi:10.1016/j.chemgeo.2007.01.004

Therefore, knowledge of the mantle argon isotope systematics can provide further constraints on the extent of degassing of different mantle reservoirs, and calculated residence times of ^{40}Ar can contribute information on mantle convection scenarios (e.g. Allègre et al., 1996; Albarède, 1998). However, a nearly ubiquitous contamination of mantle-derived rocks by atmospheric argon with its relative to mantle rocks high concentration of ^{36}Ar and low $^{40}Ar/^{36}Ar$ ratio of 295.5 significantly challenges deconvolution of mantle source compositions.

In spite of such limitations, numerous studies showed that $^{40}Ar/^{36}Ar$ ratios of specific mantle sources are significantly higher than the atmospheric ratio. Furthermore, the mantle source of ocean island basalts (OIB) and continental high-$^{3}He/^{4}He$ 'plumes' appear to have lower $^{40}Ar/^{36}Ar$ ratios (c. 5000–11,000, Marty et al., 1998; Trieloff et al., 2000; Harrison et al., 2003; Hopp and Trieloff, 2005) than the source of mid-ocean ridge–basalt (MORB) glasses (c. 20,000 to 40,000, Jambon et al., 1985; Staudacher et al., 1989; Marty and Humbert, 1997; Burnard et al., 1997; Moreira et al., 1998; Trieloff et al., 2003).

The highest $^{40}Ar/^{36}Ar$ ratios found in samples of the subcontinental lithospheric mantle (SCLM) are intermediate: 16,000–17,000 in peridotites from Massif Central/France (Dunai and Baur; 1995), from the Eifel/Germany, from the Pannonian Basin/Hungary (Buikin et al., 2005), and from the Cameroon volcanic chain (highest value of 16,300±1000 obtained by single grain laser step heating, Barfod et al., 1999), 11,000 in garnet pyroxenites from the Newer Volcanics/Australia (Matsumoto et al., 2000). Only in African diamonds derived from an old cratonic mantle lithosphere very radiogenic $^{40}Ar/^{36}Ar$ ratios>30,000 had been registered (Wada and Matsuda, 1998). In contrast, samples related to subduction zone settings tend to show significantly lowered $^{40}Ar/^{36}Ar$ ratios, commonly attributed to admixing of subduction related fluids with an atmosphere-type Ar composition (e.g. Matsumoto et al., 2001; Yamamoto et al., 2004).

The evaluation of mantle source argon isotopic compositions and their application to modelling mantle evolution needs proper deconvolution of mantle argon and atmospheric argon from variable sources, e.g. simply unfractionated air (Ballentine and Barfod, 2000) and fractionated air, e.g. related to subduction processes (Sarda, 2004). This needs concomitant precise Ne isotope measurements and the evaluation of $^{20}Ne/^{22}Ne$–$^{40}Ar/^{36}Ar$ isotope correlations. This has been done only rarely for oceanic mantle sources (Moreira et al., 1998; Trieloff et al., 2000, 2002; Hopp and Trieloff, 2005) or subcontinental volcanics (Marty et al., 1998). Buikin et al. (2005) performed high-precision measurements of $^{20}Ne/^{22}Ne$ and $^{40}Ar/^{36}Ar$ ratios on European mantle xenoliths to correct for atmospheric contributions. Their results indicate mixing between several subcomponents (asthenospheric/lithospheric, and 'plume'-related noble gases) that in addition could have experienced some degree of Ar–Ne elemental fractionation.

Another approach to assess mantle-$^{40}Ar/^{36}Ar$ ratios are high-resolution stepwise heating analyses. Argon contributions from distinct phases that are either of different origin or are more or less prone to atmospheric contamination are resolved (Trieloff et al., 1997; Hopp and Trieloff, 2005). As a consequence, sample specific maximum values might approximate the composition of the trapped mantle-$^{40}Ar/^{36}Ar$-component most closely, or at least set effective lower limits.

In this study we report the results of argon analyses on seven ultramafic rocks of the SCLM of the Red Sea region (Fig. 1, Tables 1 and 2), that is characterized by

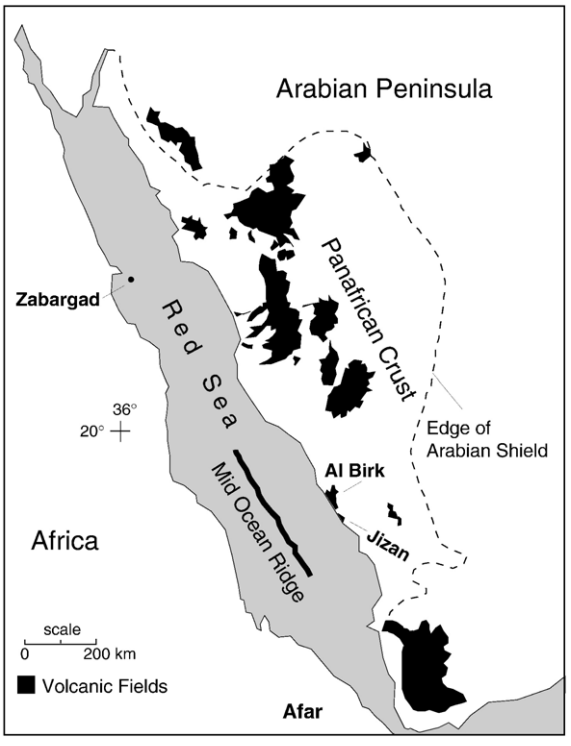

Fig. 1. Simplified map of the Red Sea region showing the sample locations and the extension of the Arabian shield that had been consolidated in Pan African times. In addition, the locations of the currently active Mid-Ocean Ridge and of the Afar hotspot are displayed.

Table 1
Ar isotopic compositions of neutron-irradiated samples

T [°C]	^{40}Ar	^{40}Ar/^{36}Ar	^{40}Ar/^{39}Ar	Apparent age [Ma]
Z 13A #4 whole rock; 670.4 mg; t_I=1 d; K=38±1 ppm				
350	44.3[a]	614 (18)	3740 (137)	1436 (36)
450	44.7[a]	931 (27)	3757 (102)	1440 (27)
550	47.3[a]	1190 (30)	4367 (167)	1594 (40)
630	55.7[a]	1640 (50)	3241 (78)	1299 (22)
710	35.9[a]	1530 (40)	1840 (90)	846 (33)
790	34.6[a]	1590 (50)	4272 (191)	1571 (47)
870	72.6[a]	4650 (230)	13,906 (577)	3083 (61)
950	165.4[a]	14,380 (780)	169,422 (37,660)	7265 (394)
1020	41.1[a]	9130 (670)	26,995 (3308)	4114 (199)
1080	21.6[a]	8310 (690)	6550 (293)	2058 (55)
1140	37.0[a]	11,940 (860)	7457 (208)	2221 (36)
1200	24.2[a]	14,240 (2560)	8005 (440)	2313 (72)
1260	61.9[a]	14,740 (1480)	29,292 (3150)	4246 (176)
1320	84.2[a]	13,370 (2980)	38,152 (20,413)	4683 (893)
1400	61.6[a]	12,080 (4030)	39,980 (35,557)	4761 (1499)
1480	62.9[a]	8390 (1350)	48,059 (9758)	5072 (344)
1560	70.5[a]	4970 (810)	34,703 (3309)	4525 (158)
1640	100.1[a]	4910 (1230)	74,628 (34,711)	5826 (806)
1700	2.7[a]	–	–	–
Total	1068.3[a]	3110 (90)	12,224 (334)	2752 (170)
−870	335.1[a]	1315 (20)		
950–1480	559.9[a]	12,041 (700)		
>1480	173.3[a]	4931 (1120)		
Z31 #2 whole rock; 481.0 mg; t_I=2 d; K=221±6 ppm				
520	64.1[a]	4480 (730)	27,071 (5035)	5317 (318)
590	194.0[a]	4530 (750)	17,505 (2003)	4581 (190)
650	560.0[a]	2980 (370)	9941 (861)	3665 (136)
700	69.5[a]	2330 (50)	2227 (156)	1642 (76)
760	299.0[a]	3760 (70)	1282 (83)	1115 (54)

Table 1 (*continued*)

T [°C]	^{40}Ar	^{40}Ar/^{36}Ar	^{40}Ar/^{39}Ar	Apparent age [Ma]
Z31 #2 whole rock; 481.0 mg; t_I=2 d; K=221±6 ppm				
810	53.1[a]	3160 (130)	1042 (107)	952 (76)
860	39.4[a]	2780 (100)	1140 (87)	1020 (60)
910	114.4[a]	2900 (90)	1260 (85)	1100 (56)
960	127.7[a]	4090 (70)	1378 (21)	1175 (13)
1000	89.0[a]	4520 (90)	840 (10)	802 (8)
1040	96.2[a]	4130 (90)	1056 (15)	962 (11)
1080	117.7[a]	4130 (60)	1611 (22)	1316 (13)
1120	160.7[a]	4110 (60)	1986 (27)	1522 (14)
1160	89.2[a]	4390 (90)	2689 (55)	1853 (24)
1200	53.7[a]	2930 (70)	2621 (83)	1824 (36)
1240	74.5[a]	2790 (50)	4938 (182)	2628 (51)
1280	135.7[a]	965 (10)	5535 (172)	2788 (44)
1310	99.5[a]	2320 (50)	4722 (236)	2567 (68)
1340	135.2[a]	3170 (70)	6877 (268)	3103 (58)
1370	90.5[a]	2290 (70)	7477 (520)	3228 (105)
1400	92.4[a]	4260 (260)	13,213 (1340)	4119 (164)
1440	171.7[a]	5400 (320)	15,715 (1194)	4403 (125)
1480	209.9[a]	5690 (450)	16,720 (1190)	4505 (118)
1510	20.5[a]	990 (210)	–	–
1550	34.7[a]	440 (50)	–	–
Total	3,192.0[a]	2930 (70)	3085 (66)	1882 (35)
Z34 #3 whole rock; 887.3 mg; t_I=2 d; K=72±3 ppm				
320	1.7[a]	1550 (570)	1207 (751)	1065 (500)
410	16.2[a]	2190 (220)	1899 (189)	1476 (100)
500	25.8[a]	2430 (230)	5778 (1071)	2849 (265)
590	55.2[a]	2710 (240)	5404 (469)	2754 (123)
680	54.3[a]	2590 (230)	10,807 (1927)	3797 (283)
770	37.3[a]	4720 (500)	7826 (1340)	3297 (259)

Table 1 (*continued*)

T [°C]	^{40}Ar	^{40}Ar/^{36}Ar	^{40}Ar/^{39}Ar	Apparent age [Ma]
Z34 #3 whole rock; 887.3 mg; t_I=2 d; K=72±3 ppm				
860	62.4 [a]	7900 (840)	6888 (1176)	3106 (253)
950	91.4 [a]	11,280 (1180)	4084 (125)	2371 (40)
1030	91.5 [a]	7890 (720)	954 (15)	888 (11)
1080	36.2 [a]	7540 (900)	399 (6)	426 (6)
1140	23.5 [a]	10,680 (2040)	720 (22)	707 (18)
1220	35.7 [a]	7290 (860)	1273 (47)	1109 (30)
1290	49.0 [a]	8310 (740)	2458 (125)	1751 (57)
1360	58.1 [a]	9080 (880)	5263 (455)	2717 (121)
1420	44.3 [a]	7910 (870)	11,581 (2771)	3907 (382)
1480	95.5 [a]	9180 (750)	240,869	9174 (3303)
1550	124.4 [a]	7680 (560)	150,764	8335 (1762)
1620	289.4 [a]	7110 (410)	266,650	9356 (1540)
1700	129.4 [a]	2070 (140)	166,849	8517 (3497)
1750	2.6 [a]	490 (560)	–	–
Total	1324.0 [a]	5070 (160)	3937 (113)	2246 (554)
Z36 #3 whole rock; 567.8 mg; t_I=1 d; K=618±5 ppm				
350	0.1 [a]	500 (707)	–	–
450	2.3 [a]	605 (55)	–	–
550	26.9 [a]	590 (8)	3338 (301)	1326 (85)
650	30.3 [a]	876 (14)	3103 (128)	1259 (38)
750	102.7 [a]	977 (11)	8851 (399)	2445 (60)
840	219.4 [a]	2780 (60)	18,591 (846)	3522 (71)
920	139.3 [a]	4090 (100)	3958 (59)	1492 (15)
980	55.9 [a]	3230 (100)	777 (10)	406 (5)
1040	53.4 [a]	3110 (140)	393 (4)	217 (2)
1100	83.4 [a]	4190 (240)	240 (2)	136 (1)
1160	45.7 [a]	4010 (460)	93 (1)	54 (1)
1240	22.3 [a]	1580 (90)	209 (4)	119 (2)
1340	42.7 [a]	1420 (80)	156 (2)	89 (1)

Table 1 (*continued*)

T [°C]	^{40}Ar	^{40}Ar/^{36}Ar	^{40}Ar/^{39}Ar	Apparent age [Ma]
Z36 #3 whole rock; 567.8 mg; t_I=1 d; K=618±5 ppm				
1450	36.4 [a]	1690 (270)	953 (35)	487 (16)
1550	74.3 [a]	2150 (530)	7306 (873)	2195 (152)
1650	126.8 [a]	2350 (750)	13,584 (3047)	3048 (475)
Total	1062.0 [a]	2030 (80)	756 (8)	355 (19)
SA87-6/9 #4 whole rock; 536.6 mg; t_I=3 d; K≈6 ppm				
350	1.2 [a]	305 (42)	–	–
500	2.1 [a]	306 (26)	–	–
650	1.0 [a]	343 (53)	30 (19)	50 (31)
800	7.0 [a]	574 (21)	726 (28)	932 (28)
950	2.3 [a]	745 (80)	1006 (107)	1192 (93)
1080	12.3 [a]	1,350 (50)	3262 (198)	2517 (83)
1200	106.8 [a]	4260 (100)	28,461 (2309)	5979 (141)
1280	75.4 [a]	3540 (160)	11,891 (987)	4493 (137)
1360	76.7 [a]	4310 (270)	12,891 (1343)	4628 (174)
1450	39.5 [a]	2500 (350)	33,107 (8745)	6242 (462)
1550	17.5 [a]	–	15,793 (5884)	4968 (630)
1650	24.2 [a]	–	97,486	8153 (4553)
Total	366.0 [a]	2940 (130)	10,368 (360)	4095 (404)

All data are calibrated against an air standard and corrected for mass discrimination and system blank (with the isotopic composition of air and 20% absolute uncertainty). Data are corrected for irradiation induced interference reactions. t_I corresponds to sample specific irradiation time. 1σ-uncertainties include uncertainties of corrections and are given in brackets. Systematic uncertainty of the amount of our calibration gas is of the order of 10%. Where no values are given, concentrations of ^{36}Ar or ^{39}Ar were below the detection limit. For Z13A#4 we additionally show total ^{40}Ar concentrations and averaged ^{40}Ar/^{36}Ar ratios of respective temperature ranges comparable to sample Z13A#3 in Table 2.

[a] [10^{-9} ccm STP/g].

the occurrence of asthenospheric, lithospheric and (Afar) plume-related components (e.g. Altherr et al., 1990; Volker et al., 1993, 1997; Hopp et al., 2004). We applied both approaches, high resolution stepwise heating Ar–Ar analyses and stepwise crushing noble gas measurements that should facilitate the determination

Table 2
Ar isotopic compositions of non-irradiated samples

Extraction	^{40}Ar [a]	$^{40}Ar/^{36}Ar$	$^{20}Ne/^{22}Ne$ [b]	$^{36}Ar/^{22}Ne$	$^{4}He/^{40}Ar$ [c]
Z13A #1 whole rock; 2.4830 g					
25 ×	1.7	5820 (130)	10.92 (2.30)	24.2 (5.2)	0.27
125 ×	12.6	6620 (150)	10.36 (29)	24.9 (0.9)	0.26
525 ×	52.1	6300 (160)	10.99 (9)	25.5 (0.6)	0.32
1800 ×	62.4	5700 (130)	11.11 (10)	32.5 (1.0)	0.35
Total	128.8	6020 (170)	10.98 (8)	28.6 (0.5)	0.33
Z13A #2 whole rock; 7.9278 g					
200 ×	33.4	8130 (140)	11.16 (6)	19.7 (0.3)	0.32
1000 ×	76.0	8470 (120)	11.50 (5)	20.1 (0.3)	0.34
2000 ×	41.0	7990 (50)	11.55 (6)	24.7 (0.4)	0.30
3000 ×	13.8	4630 (60)	11.38 (12)	44.3 (0.8)	0.29
4000 ×	6.5	3660 (70)	11.11 (28)	54.3 (1.6)	0.27
5000 ×	4.5	3730 (80)	n.a.	n.a.	n.a.
6000 ×	3.0	3320 (70)	n.a.	n.a.	n.a.
7000 ×	2.3	3480 (70)	n.a.	n.a.	n.a.
Total	180.5	7020 (80)	11.42 (10)	26.7 (0.2)	0.30
Z13A #3 whole rock; 2.4277 g					
850 °C	32.7	1210 (20)	10.74 (22)	175.0 (4.4)	0.19
1450 °C	70.2	11,220 (270)	12.06 (22)	30.2 (0.8)	0.30
1650 °C	34.9	4900 (120)	10.33 (18)	15.7 (0.9)	0.29
Total	137.8	3410 (90)	10.85 (18)	49.6 (0.9)	0.28
Z31 #1 whole rock; 2.4398 g					
20 ×	17.1	1850 (30)	10.12 (14)	50.1 (0.8)	0.14
60 ×	26.6	1910 (30)	10.32 (10)	52.4 (0.7)	0.14
180 ×	59.4	2200 (20)	10.44 (6)	45.7 (0.5)	0.15
680 ×	155.7	2800 (30)	10.67 (4)	52.5 (0.7)	0.13
1680 ×	92.2	3420 (40)	11.09 (9)	45.8 (0.7)	0.15
Total	351.0	2640 (30)	10.64 (4)	49.4 (0.4)	0.14
Z34 #1 whole rock; 7.9380 g					
200 ×	34.8	5470 (160)	10.60 (7)	26.7 (0.2)	0.16
1000 ×	64.7	6030 (180)	10.76 (4)	26.8 (0.2)	0.19
2000 ×	33.7	6470 (180)	10.89 (6)	27.9 (0.2)	0.18
3000 ×	14.6	6390 (180)	10.83 (16)	32.7 (0.5)	0.18
4000 ×	7.2	5190 (180)	10.96 (22)	41.3 (0.9)	0.19
Total	155.0	5970 (100)	10.76 (10)	27.9 (0.1)	0.18
Z36 #1 whole rock; 7.5061 g					
200 ×	18.2	1450 (20)	10.14 (5)	28.2 (0.8)	0.98
1000 ×	32.7	1750 (20)	10.36 (5)	27.9 (0.8)	1.10
2000 ×	12.0	1720 (10)	10.50 (6)	35.0 (1.0)	1.14
3000 ×	3.5	1820 (20)	10.55 (12)	38.3 (0.5)	1.16
4000 ×	2.1	1770 (40)	10.11 (29)	38.3 (1.2)	1.23
Total	68.5	1660 (40)	10.31 (11)	29.6 (0.5)	1.08
SA87-6/9 #1 px; 2.1417 g					
250 ×	9.6	2260 (50)	10.74 (45)	34.5 (1.4)	0.41
1750 ×	34.6	3520 (70)	11.11 (16)	30.3 (0.5)	0.40
Total	44.1	3140 (60)	11.01 (19)	31.5 (0.5)	0.40
SA87-6/9 #2 whole rock; 11.1754 g					
200 ×	4.2	519 (23)	9.81 (5)	28.4 (0.4)	0.65
1000 ×	8.8	633 (28)	9.97 (3)	28.4 (0.4)	0.64
2000 ×	4.9	726 (32)	9.99 (4)	31.5 (0.4)	0.60

Table 2 (*continued*)

Extraction	^{40}Ar [a]	$^{40}Ar/^{36}Ar$	$^{20}Ne/^{22}Ne$ [b]	$^{36}Ar/^{22}Ne$	$^{4}He/^{40}Ar$ [c]
SA87-6/9 #2 whole rock; 11.1754 g					
3000 ×	2.6	666 (29)	9.98 (6)	35.0 (0.5)	0.57
Total	20.6	628 (16)	9.93 (7)	29.7 (0.2)	0.62
SA87-6/9 #3 px; 8.0104 g					
200 ×	9.7	2060 (20)	10.25 (5)	20.4 (0.1)	0.45
1000 ×	18.7	2810 (30)	10.48 (5)	18.5 (0.1)	0.45
2000 ×	10.8	3570 (20)	10.71 (8)	20.1 (0.2)	0.42
4000 ×	7.5	4230 (100)	11.00 (7)	22.9 (0.2)	0.36
Total	46.7	2890 (20)	10.51 (3)	19.8 (0.1)	0.43
SA 87-2/12 #1 cpx; 8.9221 g					
150 ×	192.6	3380 (10)	10.14 (2)	10.2 (0.1)	0.22
550 ×	269.7	6790 (30)	10.43 (2)	8.6 (0.1)	0.23
1000 ×	266.1	9280 (40)	10.52 (3)	11.8 (0.2)	0.13
1500 ×	132.7	12,710 (70)	10.71 (3)	9.3 (0.1)	0.14
2100 ×	111.7	14,700 (100)	10.81 (4)	12.2 (0.2)	0.09
3000 ×	70.5	16,500 (180)	10.94 (4)	9.6 (0.1)	0.10
4800 ×	66.4	20,670 (300)	11.22 (4)	9.4 (0.1)	0.08
7300 ×	45.0	25,590 (620)	11.34 (6)	8.9 (0.1)	0.07
9800 ×	15.9	24,840 (510)	11.17 (11)	8.4 (0.2)	0.08
Total	1170.6	7640 (60)	10.41 (4)	9.9 (0.1)	0.16
SA 86-121/1 #1 cpx; 7.8410 g					
200 ×	63.6	1830 (10)	9.97 (2)	13.6 (0.2)	0.60
500 ×	61.0	3090 (50)	10.03 (2)	15.9 (0.2)	0.42
900 ×	35.6	3570 (20)	10.04 (3)	13.8 (0.2)	0.49
1700 ×	42.1	4600 (30)	10.16 (4)	13.1 (0.2)	0.47
3200 ×	25.3	6490 (50)	10.37 (6)	18.0 (0.3)	0.30
3800 ×	7.1	7690 (290)	10.53 (16)	15.5 (0.3)	0.32
Total	234.7	2990 (30)	10.04 (2)	14.3 (0.1)	0.48

Z13A#3 was fused by low resolution stepwise heating extraction. Uncertainties as described in Table 1.
'×' indicates cumulative number of strokes. n.a. not analysed.
[a] In 10^{-8}ccm STP/g.
[b] Hopp et al., 2004.
[c] Corrected for atmospheric ^{40}Ar.

of more reliable sample specific mantle-$^{40}Ar/^{36}Ar$ ratios.

2. Geology and samples

The Red Sea is a young rift graben of c. 3000 km length (Fig. 1). It follows a former suture, the Nubian–Arabian Shield that formed during the Pan African orogenic event c. 700 Ma ago. The sampled lithospheric mantle is of the same age, as indicated by dating of ultramafic rocks that suffered only marginal late modification via metasomatic events (Brueckner et al., 1988; Henjes-Kunst et al., 1990; Brueckner et al., 1995). After long time of tectonic quiescence continental rifting started about 30 Ma ago in the southern part around the Afar area, accompanied or initiated by the extensive extrusion of the Ethiopian flood basalts. The latter is mostly related to the impact of a mantle 'plume', which is sustained by observed high $^{3}He/^{4}He$ ratios typically found also at oceanic hotspot locations (Marty et al., 1996; Scarsi and Craig, 1996). Contemporaneously or soon after onset of the volcanic activity, continental rifting started along the whole today rift graben. In course of proceeding lithospheric thinning, tectonic uplift led to rapid exhumation of a small portion of mantle lithosphere intruding into the overlying crust and sediments at c. 20 Ma ago associated with extensive contact metamorphism (Nicolas and Boudier, 1987; Kurat et al., 1993; Trieloff et al., 1997; Bosch and Bruguier, 1998). Because of this rapid uplift three exceptionally fresh peridotite bodies consisting mainly of spinel lherzolites, with minor occurrence of harzburgites, dunites and vein rocks are now exposed at the island of Zabargad in the northern Red Sea (Fig. 1). Basalt dikes of Quaternary age are widely found at the Main Peridotite Hill (MPH) in the southern part of the

island, whereas the Northern and Central Peridotite Hill (NPH, CPH) seem not or less affected of such late activity. The four samples used for this study had been collected from all three peridotite bodies by Gero Kurat and co-workers at a cruise in 1980 (Kurat et al., 1993).

The oceanic phase of the Red Sea basin started c. 10 Ma ago with the opening of the Gulf of Aden and propagated to north c. 5 Ma ago. This extension is accompanied by volcanism mainly on the Arabian rift shoulder extending over the whole length from Yemen to Syria. The lithospheric mantle suffered local melt metasomatism, as documented by the occurrence of glass and secondary amphiboles in a sub-suite of Arabian mantle xenoliths (Henjes-Kunst et al., 1990). Similarly, Nd–Sr isotope data were interpreted to reflect remobilization of an enriched mantle-type and isotopically homogenized melt from deeper to shallower levels (Henjes-Kunst et al., 1990). However, most investigated xenoliths studied by Henjes-Kunst et al. (1990) do only evidence minor metasomatic reactions, including the xenolith samples analysed for this study. These xenoliths had been collected from Quaternary basanites at the volcanic fields Al Birk and Jizan in the southern part of the Red Sea region (Fig. 1).

All samples equilibrated under typical lithospheric mantle conditions at c. 800–1100 °C and in the spinel–plagioclase stability field, i.e. at c. 0.5–1.5 GPa. A detailed description including microprobe results of the Zabargad samples is given in Brandstaetter et al. (1993), from which we adopted a short description here. Z13A (MPH) is a fresh, coarse-grained spinel lherzolite with porphyroclastic texture. It is classified as primitive, slightly depleted peridotite (Kurat et al., 1993). Vein rock Z31 (CPH) is a very coarse-grained orthopyroxenite with minor amounts of olivine and spinel. Spinel plagioclase lherzolite Z34 (CPH) is a coarse-grained rock with porphyroclastic texture and interstitially contains brown amphibole. As Z13A, it is classified as primitive peridotite by Kurat et al. (1993). Z36 (NPH) is a foliated amphibole dunite and contains large porphyroblasts of green amphibole along the foliation plane. Apatite and orthopyroxene are present in small amounts in the matrix. This rock is considered as metasomatized peridotite in course of the tectonic emplacement of Zabargad and is enriched in incompatible elements (e.g. U, Th) and depleted in magmatophile major elements (Kurat et al., 1993).

Xenolith SA 86-121/1 from Jizan is a spinel- and phlogopite-bearing websterite with very minor amounts of olivine. The rock is characterized by a granoblastic texture. Both pyroxenes contain exsolution lamellae of each other and abundant fluid inclusions. Sample SA 87-2/12 (Al Birk) is a spinel- and olivine-bearing websterite with a heterogranular to weakly porphyroclastic texture. Both, clino- and orthopyroxene are anhedral and are present in approximately equal amounts. Olivine and spinel occur as intergranular phases and are inclusions in pyroxene. Clinopyroxene displays exsolution lamellae of orthopyroxene and ilmenite, while orthopyroxene contains only ilmenite. SA 87-6/9 (Al Birk) is a heterogranular to weakly porphyroclastic spinel lherzolite. Olivine has kink bands, and pyroxenes do not show exsolution lamellae.

All samples are part of a larger sample suite of ultramafic rocks from the Red Sea region that had been pre-investigated for their Ar isotopic composition and concentration. The samples presented in this study are those chosen because of their high amounts of mantle argon and, therefore, had also been selected for combined He–Ne–Ar analyses.

Due to their relatively gas rich nature it is not surprising to find abundant trails of fluid inclusions in these rocks. Fluid inclusion assemblages are secondary, with the trails frequently crossing grain boundaries, but partly are also restricted to single grains. In all samples, either the inclusion sizes are too small or opacity is too high for a microthermometric analysis.

3. Experimental methods

The argon isotopic composition of five neutron-irradiated whole-rock samples had been analysed using extractions by high resolution stepwise heating in an inductively heated furnace (Table 1). According to the $^{40}Ar/^{39}Ar$ dating technique, we obtained information about possible *in-situ* production of $^{40}Ar^*$. Throughout this article the expression *in-situ* refers to accumulation of radiogenic $^{40}Ar^*$ since the time the respective mineral phase can be treated as closed system regarding Ar, regardless whether closure occurred under lithospheric mantle conditions or during crustal residence. An upper age limit is set by the local lithosphere formation age of c. 700 Ma (Brueckner et al., 1988; Henjes-Kunst et al., 1990; Brueckner et al., 1995). Initially, measured argon isotopic compositions and degassing behaviour were anticipated to yield a 'best suited' sample specific heating schedule for noble gas measurements, mainly because less extractions are required to reach high precision in helium and neon analyses. Experimental limitations allowed this ideal approach for Z13A only (Table 2), similarly Ar high-resolution stepwise heating analyses were precluded for the remaining two xenoliths SA 86-121/1 and SA 87-2/12. Therefore, with exception of Z13A, for all samples concomitant data of He, Ne and Ar are only obtained by the stepwise crushing method. In spite of these

'shortcomings', our data sets are more complete than in comparable studies, and we show that the additional use of Ar high resolution stepheating valuably supplement He–Ne–Ar stepcrush data in order to substantiate conclusions about mantle argon endmember compositions.

The samples were neutron-irradiated without Cd-shielding in the GKSS-reactor in Geesthacht, Germany. For correction of interfering isotopes we used 2.66 Ga old NL25-hornblende (Schaeffer and Schaeffer, 1977) and HD-B1 biotite (24.03 Ma old, Fuhrmann et al., 1987) age monitors and CaF_2 standards. To avoid significant production of Ca-derived ^{36}Ar in our samples we restricted the irradiation time to one, two, and three days during three separate irradiations. Respective *J*-values were 0.0003, 0.0007, and 0.0009. Decay constants follow the convention recommended by Steiger and Jäger (1977).

Before crushing and fusion analyses all samples had been cleaned ultrasonically with diluted HNO_3, de-ionized water and ethanol. Details of experimental procedure for Ar–Ar measurements can be found in Trieloff et al. (1997, 2003). Combined He–Ne–Ar analyses were performed as described previously by Buikin et al. (2005). In sequential dynamic crushing experiments, noble gases were extracted by up to three simultaneously driven ball mills. System blank heights of ^{40}Ar varied between 0.2 and $1.2 \cdot 10^{-9}$ ccm STP during crushing extractions, and reached up to $1.8 \cdot 10^{-8}$ ccm STP at 1650 °C. During Ar–Ar fusion experiments, blank heights ranged from $2 \cdot 10^{-10}$ (cold) up to $5 \cdot 10^{-9}$ ccm STP/g (1650 °C). Within uncertainties the blank had the isotopic composition of air (for both methods).

4. Results

In the following subsections we evaluate high resolution stepwise heating data and set sample specific lower limits for mantle-$^{40}Ar/^{36}Ar$ ratios. Independently, we calculate mantle-$^{40}Ar/^{36}Ar$ ratios by using $^{20}Ne/^{22}Ne$ ratios as proxy for atmospheric additions from stepwise crushing experiments. Coherent values found with both approaches strongly support a successful determination of a sample specific mantle-$^{40}Ar/^{36}Ar$ ratio.

Throughout this article we refer to fluids as free, predominantly CO_2 or H_2O bearing fluid phases. To distinguish the provenance of the noble gases carried with them we use the terms atmospheric, crustal and mantle fluids, the latter further subdivided in 'plume' derived and asthenospheric/lithospheric fluids. All of these 'reservoirs' display characteristic compositions, differing in the relative proportions of their radiogenic and primordial noble gas isotopes.

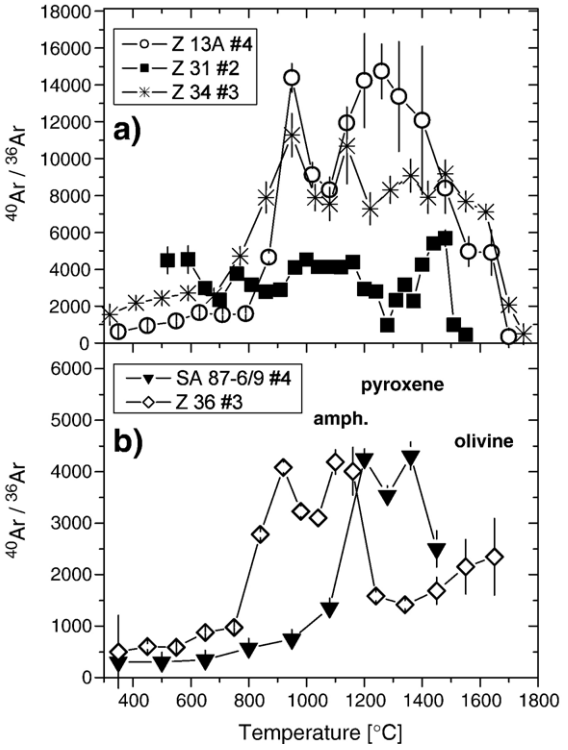

Fig. 2. $^{40}Ar/^{36}Ar$ ratios vs temperature obtained by high resolution stepwise heating analyses. All samples are whole-rock splits.

4.1. $^{40}Ar/^{36}Ar$ ratios and apparent ages obtained by high-resolution stepwise heating argon extractions

In Fig. 2a,b we plotted the $^{40}Ar/^{36}Ar$ ratios against release temperature (Table 1). The temperature schedule was chosen to ensure a good resolution of the different phases (olivine, pyroxene, accessory phases like amphibole) according to previous experiences (Trieloff et al., 1997; Hopp and Trieloff, 2005). More information about the respective release pattern can be found in the provided Supplementary material. It can be summarized that the low temperature extractions tend to show lower $^{40}Ar/^{36}Ar$ ratios, and the higher temperature extractions (here:>900 °C) exhibit higher $^{40}Ar/^{36}Ar$ ratios. Maximum ratios of individual samples vary strongly from c. 4000 (Z36#3, SA 87-6/9#4) to c. 14,000 (Z13A#4). In all samples, maximum ratios are reproduced in two or more subsequent extractions suggesting that the respective maximum $^{40}Ar/^{36}Ar$ ratios of the sample specific trapped mantle component is resolved. These highest $^{40}Ar/^{36}Ar$ ratios are not restricted to the degassing of a specific phase, though in most samples (except Z36#3) both pyroxenes are a major host phase of mantle argon with remarkably high $^{40}Ar/^{36}Ar$ ratios. In addition, we observe similar high ratios in a distinct release peak at

c. 900 °C for samples Z13A#4, Z34#3 and Z36#3, for which the host phase remains enigmatic.

Apparent ages calculated according to the ^{40}Ar–^{39}Ar technique mostly exceed the lithospheric age (c. 700 Ma) significantly (Table 1). A calculation of possible *in-situ* radiogenic $^{40}Ar^*$ accumulated in this time would only account for 4.9%, 4.2%, and 4.3% in extractions with highest sample specific $^{40}Ar/^{36}Ar$ ratios of Z13A#4 (1260 °C), Z31#2 (1480 °C), and SA 87-6/9#4 (1360 °C), respectively. The resulting corrected values would be still within the 1σ-uncertainty of the measured values. The highest $^{40}Ar/^{36}Ar$ ratio observed for Z34#3 (950 °C) would be lowered by c. 17% from 11,280 down to 9360. A correction of radiogenic $^{40}Ar^*$ applied for the high temperature extractions still yields a highest $^{40}Ar/^{36}Ar$ ratio of 9150. However, this sample has a "saddle-shaped" age spectrum (Lanphere and Dalrymple, 1976) with a minimum age of 426 Ma, that would serve as upper age limit and favours a more recent formation age of the respective K-bearing phase.

Amphibole–dunite Z36#3 exhibits a more complicated pattern. Here, the observed $^{40}Ar/^{36}Ar$ ratios at intermediate temperatures reflect a mixture of trapped ^{40}Ar and radiogenic $^{40}Ar^*$, as evidenced again by a "saddle-shaped" age spectrum (Lanphere and Dalrymple, 1976). The minimum apparent age of 54±1 Ma is interpreted as maximum value for formation of the foliated amphibole in course of intense shearing during lithospheric uplift and – taken as upper limit – would be in agreement with the c. 20 Ma age of this event (Trieloff et al., 1997; Bosch and Bruguier, 1998). Unfortunately, due to the presence of at least two distinct trapped components (mantle, atmospheric) in Z36#3 calculation of an isochrone (in a $^{40}Ar/^{36}Ar$ vs $^{39}Ar/^{36}Ar$ plot) that could further support this conclusion, failed. However, radiogenic contributions cannot account for the 920 °C and the high temperature (>1480°) extractions, since apparent ages are far above the 20 Ma emplacement age, i.e. most of the ^{40}Ar must be considered as trapped. This might be different, if again a lithosphere retention age of 700 Ma is assumed. Here, a correction of the observed maximum $^{40}Ar/^{36}Ar$ ratio of 4090±100 (920 °C) for *in-situ* radiogenic $^{40}Ar^*$ would lower this ratio by 36.1% down to 2610. A similar calculation for the 1650 °C extraction would result in a $^{40}Ar/^{36}Ar$ ratio of 2100, corresponding to a 10.6% decrease. However, it seems highly questionable if ancient phases could have survived unaffected in this particular rock. The observed highest $^{40}Ar/^{36}Ar$ ratio of 4090±100 at 920 °C seems more representative for the trapped component in Z36#3.

The He and Ne results reported previously (Hopp et al., 2004) do not evidence any contribution of crustal fluids that would be characterized by high $^{4}He/^{3}He$ and $^{21}Ne/^{22}Ne$ ratios. Thus, we suggest the trapped components with high $^{40}Ar/^{36}Ar$ ratios originated in the mantle.

The estimated lower limits of sample specific mantle-$^{40}Ar/^{36}Ar$ ratios encompass a wide range (uncertainties 1σ): 14,740±1480 (Z13A#4, 1260 °C);

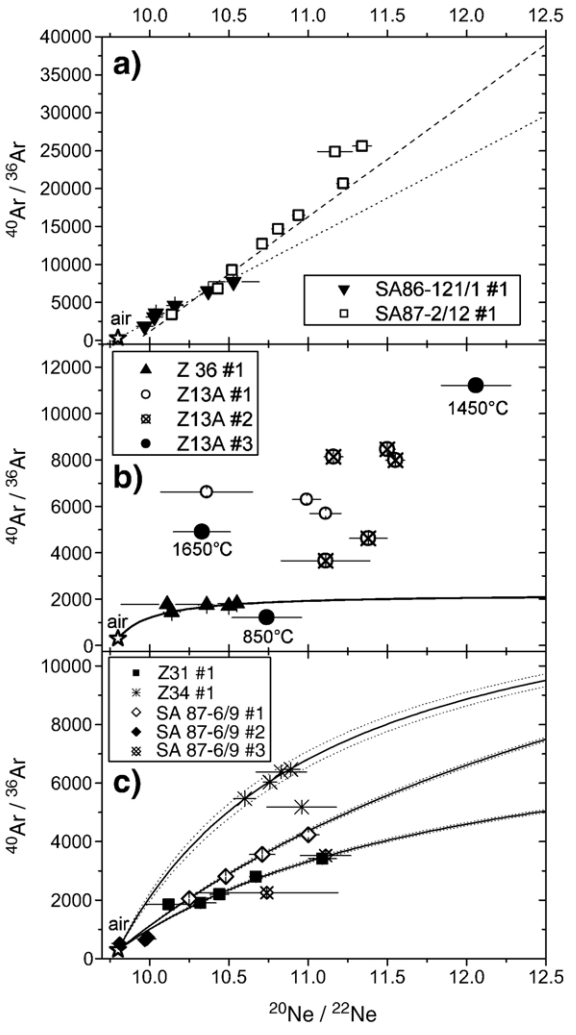

Fig. 3. Results of $^{40}Ar/^{36}Ar$ and $^{20}Ne/^{22}Ne$ ratios obtained by stepwise crushing and, in case of sample Z13A#3, by stepwise heating extractions. a) Pyroxene separates SA86-121/1 and SA87-2/12 show an approximately linear correlation. Lines represent linear fits (see text for details). b) For Z13A whole-rock, $^{40}Ar/^{36}Ar$ and $^{20}Ne/^{22}Ne$ ratios appear to be uncorrelated. Extraction temperatures of Z13A#3 are indicated. A poorly defined mixing hyperbola with a mantle-$^{40}Ar/^{36}Ar$ ratio of about 2090±20 was calculated for Z36 whole rock. c) For whole-rock splits Z31#1, Z34#1, and pyroxene separate SA87-6/9#3 we were able to compute rather well defined mixing hyperbolas that yielded mantle-$^{40}Ar/^{36}Ar$ ratios of 5040±50, 9510±220, and 7500±70, respectively. Data for another px-separate SA 87-6/9#1 and whole-rock SA 87-6/9#2 are also shown.

11,280±1180 (Z34#3, 950 °C); 5690±450 (Z31#2, 1480 °C); 4310±270 (SA87-6/9#4, 1360 °C); and 4090±100 (Z36#3, 920 °C).

4.2. Results of simultaneous measurements of argon and neon isotopes

$^{40}Ar/^{36}Ar$ ratios of the crushed samples from Zabargad Island (Z13A#1, #2, Z31#1, Z34#1, Z36#1; Fig. 3b,c; Table 2) are generally lower than values obtained by high-resolution stepwise heating extractions. Possibly, stepwise crushing of whole-rock samples might not have resulted in a separation of high and low $^{40}Ar/^{36}Ar$ mineral phases. Such a separation may have been more successful in the case of the low resolution stepwise heating analyses of Z13A#3 (Table 2), as $^{40}Ar/^{36}Ar$ ratios are almost identical to the averaged values observed at respective temperature ranges in Z13A#4 (Table 1). On the other hand, the maximum $^{40}Ar/^{36}Ar$ ratio of the pyroxene separate from spinel lherzolite SA87-6/9#3 obtained by crushing was 4230±100 (Table 2, Fig. 3c), similar to the result of stepwise heating (Table 1, Fig. 2b). This suggests that in the case of pyroxene (which is enriched in mantle argon) stepcrushing extractions yielded a similarly well mantle argon resolution as stepwise heating.

Two more samples had been analysed by stepcrushing, for which no high resolution stepheating measurements are available: Websterites SA 87-2/12 and SA 86-121/1, for which we obtained maximum $^{40}Ar/^{36}Ar$ ratios of 25,590±620 and 7690±290, respectively (Fig. 3a). The former value is the highest measured value for a pyroxenite/peridotite rock so far. To exclude a possible contribution of *in-situ* radiogenic $^{40}Ar^*$ hosted in glass pockets (SA87-2/12) or minute amounts of phlogopite (SA86-121/1), we determined the K concentrations in these two samples photometrically on the powders that were left after crushing and obtained for both samples a value of 70±20 ppm (upper limit). Even assuming Ar closure since a Pan African lithosphere age of 700 Ma this would result in a contribution of 2.7% and 11.3% *in-situ* radiogenic $^{40}Ar^*$, provided all radiogenic lattice sited $^{40}Ar^*$ could be released, which is doubtful. Therefore, we consider the $^{40}Ar/^{36}Ar$ composition as a property of the trapped mantle component.

4.3. Determination of mantle-$^{40}Ar/^{36}Ar$ ratios by calculating mixing hyperbola

Since all samples analysed in this study show a clear addition of atmospheric neon (Hopp et al., 2004), low $^{40}Ar/^{36}Ar$ ratios in the analysed mantle rocks are not necessarily a characteristic of the incorporated mantle component, but only serve as a lower limit. In case of a simple two-component mixture between a mantle and an atmospheric endmember we should observe a hyperbolic correlation in an $^{40}Ar/^{36}Ar$–$^{20}Ne/^{22}Ne$ isotope space (Eq. (1), after Langmuir et al., 1978):

$$\left(\frac{^{40}Ar}{^{36}Ar}\right) = \frac{-\left(\left(\left(\frac{^{40}Ar}{^{36}Ar}\right)_M \cdot r - \left(\frac{^{40}Ar}{^{36}Ar}\right)_A\right)\cdot\left(\frac{^{20}Ne}{^{22}Ne}\right) + \left(\frac{^{40}Ar}{^{36}Ar}\right)_A \cdot \left(\frac{^{20}Ne}{^{22}Ne}\right)_M - r\cdot\left(\frac{^{40}Ar}{^{36}Ar}\right)_M \cdot \left(\frac{^{20}Ne}{^{22}Ne}\right)_A\right)}{\left((1-r)\cdot\left(\frac{^{20}Ne}{^{22}Ne}\right) - \left(\frac{^{20}Ne}{^{22}Ne}\right)_M + r\cdot\left(\frac{^{20}Ne}{^{22}Ne}\right)_A\right)}. \quad (1)$$

The curvature of such a mixing hyperbola is defined by the ratio r of the corresponding endmember $^{36}Ar/^{22}Ne$ ratios (subscripts M = mantle, A = atmosphere). Application of a least square fitting routine allows calculation of a best sample-specific mixing hyperbola.

Table 3
Parameters of optimized mixing hyperbola for samples Z31, Z34, Z36, and SA87-6/9 #3

Sample	χ^2_{Total}	R^2	$r_{EXTR.}$	$^{40}Ar/^{36}Ar_{EXTR.}$	$^{40}Ar/^{36}Ar_{MAX.\ OBS.}$	$^{21}Ne/^{22}Ne_M$ [a]
Z31 #1 [b]	2.95	0.975	2.19 (5)	5040 (50)	5690 (450)	0.0529 (17)
Z34 #1 [c]	0.09	0.989	3.03 (20)	9510 (220)	11,280 (1180)	0.0554 (26)
Z36 #1	9.41	0.904	12.8	2090 (20)	4090 (100)	0.0562 (27)
SA87-6/9 #3	0.95	0.933	1.62 (3)	7500 (70)	4310 (270)	0.0565 (27)
SA87-2/12 [d]	–	0.986	–	39,000 (2500)	25,590 (620)	0.0569 (10)
SA86-121/1 [d]	–	0.987	–	29,600 (2700)	7690 (290)	0.0675 (51)

R^2 is the correlation coefficient. The calculated values and 1σ-uncertainties of the curvature parameter r_{EXTR} and mantle-$^{40}Ar/^{36}Ar_{EXTR}$ at $^{20}Ne/^{22}Ne=12.5$ are shown and compared with maximum $^{40}Ar/^{36}Ar_{MAX.OBS}$ ratios estimated from results of high resolution stepwise heating extractions. Uncertainty of r for Z36 was not constrained by the fit routine.

[a] $^{21}Ne/^{22}Ne_M$=mantle ratios extrapolated to $^{20}Ne/^{22}Ne=12.5$ (Hopp et al., 2004).

[b] Extraction 25 × had not been used for regression analyses.

[c] Extraction 4000 × had not been used for regression analyses.

[d] Results of linear fit. See text for details.

Extrapolation to a mantle-$^{20}Ne/^{22}Ne$ ratio of 12.5 (Trieloff et al., 2000, 2002; Hopp and Trieloff, 2005; Ballentine et al., 2005) then yields the respective mantle-$^{40}Ar/^{36}Ar$ ratio, that is hosted by the specific sample.

In several cases the simple assumption of a binary mixing scenario does not hold, thus making it impossible to calculate mantle compositions. From Fig. 3b, this is evident for sample Z13A. The Ar–Ne data obtained for samples SA86-121/1 and SA87-2/12 (Fig. 3a) seem to be approximately linearly correlated (equivalent to a mixing hyperbola with $r \approx 1$). A hyperbola least square fit diverged. Application of a linear fit resulted in mantle-$^{40}Ar/^{36}Ar$ ratios of c. 39,000±2500 (SA 87-2/12, air point not included in fit) and 29,600±2700 (SA 86-121/1, air point included in fit).

For sample Z36#1, the best fit hyperbolic mixing line yields a mantle-$^{40}Ar/^{36}Ar$ ratio of 2090±20 (Fig. 3b, Table 3). The low 1σ-uncertainty is due to the very large concave curvature corresponding to a high r value of 12.8 (Table 3). Even a significant variation in r will then hardly influence the extrapolated mantle-$^{40}Ar/^{36}Ar$ ratio. The reliability of this fit is questionable as reflected in the high χ^2 value of 9.4. The extrapolated value of the mantle-$^{40}Ar/^{36}Ar$ ratio is lower as compared with the stepwise heating maximum $^{40}Ar/^{36}Ar$ ratio of 4090±100, but similar to the high temperature values (Table 1, Fig. 2b). Hence, we consider the hyperbola fit not as reliable for Z36#1.

Apparently, only for samples Z31 #1, Z34 #1, and SA 87-6/9 #3, the assumption of binary mixing seems reasonable and the calculation of mixing hyperbolae yields rather well-defined $^{40}Ar/^{36}Ar$ ratios (Fig. 3c). Results of the regression analysis are summarized in Table 3. We obtained mantle-$^{40}Ar/^{36}Ar$ ratios of 5040±50 (Z31); 9510±220 (Z34#2); and 7500±70 (SA87-6/9#3). The r values are 2.19±0.05, 3.03±0.20, and 1.62±0.03, respectively. Note, that for regression analysis the first extraction of Z31#1 and the last extraction of Z34#1 were omitted because of their relatively high uncertainties. In case of Z31#1 inclusion of this value raise the r parameter and in particular the χ^2 value, and lowers the calculated mantle-$^{40}Ar/^{36}Ar$ ratio (c. 4340±260). A regression analysis for Z34#1 with all data failed. However, both excluded data points are within 2σ-uncertainty in agreement with regression curves resulting without these points. In case of Z31 #1 and Z34 #1 the mantle-$^{40}Ar/^{36}Ar$ ratios broadly agree with the maximum $^{40}Ar/^{36}Ar$ ratios of the stepwise heating experiments (Fig. 2a, Table 3). For both samples, previous total fusion and stepwise crushing data (Trieloff et al., 1997) yielded maximum $^{40}Ar/^{36}Ar$ ratios of 5340 (Z31) and 2090 (Z34) that are similar or lower than values obtained in this study.

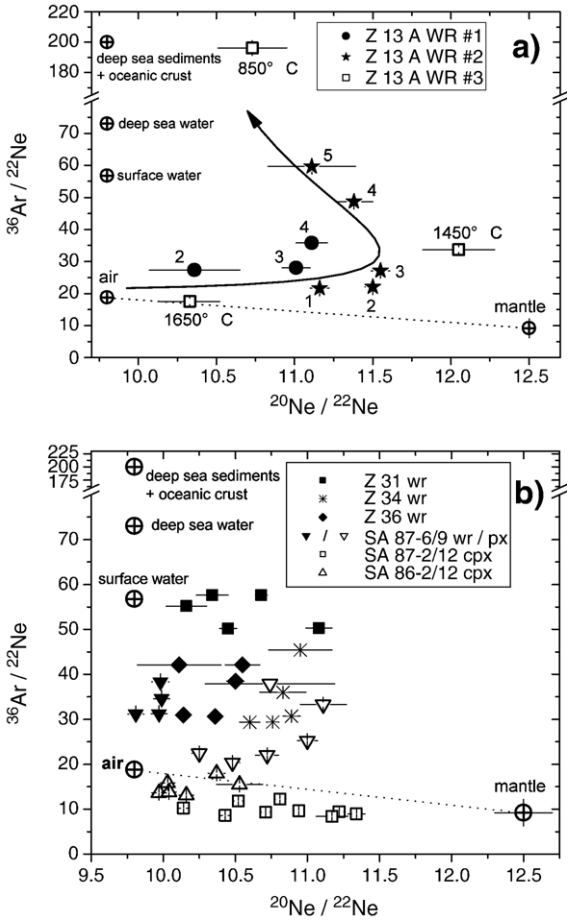

Fig. 4. $^{36}Ar/^{22}Ne$ ratios plotted against $^{20}Ne/^{22}Ne$. Postulated mantle value from Trieloff et al. (2002). Unfractionated and fractionated atmospheric compositions from Ozima and Podosek (2002). a) Splherzolite Z13A. With successive crushing steps (numbers close to symbol) composition changes from unfractionated atmosphere via dominantly mantle to strongly fractionated atmosphere. This change is indicated by arrow (first low precision crush value of Z13A#1 not shown). This is also mirrored by results of the fused split (temperatures shown in graph). b) All other samples. Filled symbols and stars represent whole-rock data; open symbols correspond to pyroxene separates. Whole rocks generally exhibit higher Ar/Ne ratios.

Maximum $^{40}Ar/^{36}Ar$ ratios measured by both heating and crushing of SA87-6/9 (Figs. 2b, 3c, Tables 1–3) are about 4300±300, i.e. significantly below the calculated mantle value of 7500±70.

The reliability of our curve fits could be principally checked by considering the $^{36}Ar/^{22}Ne$ ratios of the sample-specific atmospheric and mantle endmember components. In case of a binary mixture, the $^{36}Ar/^{22}Ne$ endmember ratios correspond to the r value and characterize the curvature of the sample's hyperbola. Unfortunately, it was not possible to determine the

respective endmember values by line fits, as the scatter in a $^{36}Ar/^{22}Ne$ vs. $^{20}Ne/^{22}Ne$ diagram (Fig. 4a,b; Table 2) was too large. Nevertheless we may roughly constrain the mantle-$^{36}Ar/^{22}Ne$ ratios: All whole-rock samples tend to show elevated $^{36}Ar/^{22}Ne$ ratios at low $^{20}Ne/^{22}Ne$ ratios, i.e. Ar-enriched atmospheric components with respect to the unfractionated $^{36}Ar/^{22}Ne$ ratio of 18.7 (Ozima and Podosek, 2002). From the concave ($r>1$) curvatures of the mixing hyperbolae of Z31#1 and Z34#1 (Fig. 3c), we thus can deduce a respective mantle-$^{36}Ar/^{22}Ne$ ratio larger than the $^{36}Ar/^{22}Ne$ ratio of the trapped atmospheric component (i.e. >20), larger than estimates for unfractionated mantle values with 9.2± 3.0 (Trieloff et al., 2002) or 8.9±0.6 (Holland and Ballentine, 2006). This also holds for pyroxene separate SA87-6/9#3 with a rather unfractionated atmospheric component, but an r-value>1. The lowest $^{36}Ar/^{22}Ne$ values are found for pyroxene separate of SA 87-2/12 and scatter at ~10 (Fig. 4b; Table 2), similar to the postulated mantle value. This sample also showed the highest measured $^{40}Ar/^{36}Ar$ ratio of all samples.

The occurrence of atmospheric noble gases with highly fractionated $^{36}Ar/^{22}Ne$ ratios and elevated mantle-$^{36}Ar/^{22}Ne$ ratios (>10) seems a general feature for many samples of the subcontinental lithospheric mantle, as evidenced by previous studies (e.g. Buikin et al., 2005). The presence of differently fractionated atmospheric components can be qualitatively explained by incorporation of altered phases involving interaction with hydrous fluids (e.g. meteoric waters, laboratory treatment). For example, Buikin et al. (2005) observed distinct atmospheric $^{36}Ar/^{22}Ne$ ratios trapped in mantle xenoliths from the same flow unit, that point to sample-specific late incorporation of variably fractionated atmospheric noble gases, whereas the respective mantle-$^{36}Ar/^{22}Ne$ was constant but higher than the oceanic value of c. 10.

4.4. Comparison of total release ^{40}Ar- fusion vs. crushing

^{40}Ar concentrations released by crushing are expected to be lower than by fusion, since crushing does not liberate argon from mineral lattices. In spite of this consideration, total concentrations observed in crushed and fused subsamples are in good agreement for Z13A, Z31, and Z34. Fused amphibole dunite Z36#3 contains some *in-situ* radiogenic $^{40}Ar^*$, that might be at least in part responsible for the observed lower gas release in the crushed sample, for which we would not expect significant contributions from lattice-sited radiogenic $^{40}Ar^*$. ^{40}Ar concentrations in both crushed pyroxene separates SA 87-6/9 #1, #3 were slightly higher compared to the fused whole-rock SA 87-6/9#4, whereas the crushed whole-rock SA 87-6/9#2 showed lower concentrations. The latter is most likely due to the profound contamination with atmospheric argon making a comparison with the other subsamples questionable that display a clear mantle argon component. In opposite, comparison of pyroxene separates and whole-rock sample SA 87-6/9 #4 requires correction on modal composition of the whole-rock sample. Taking 30% pyroxene abundance as reasonable estimate, the separates were degassed to about 50% by crushing.

We also observe a roughly parted ^{40}Ar release from lower temperature (<c. 1000 °C) and higher temperature extractions (>c. 1000 °C) for the Zabargad samples, whereas spinel lherzolite SA 87-6/9#4 predominantly degassed above 1000 °C (c. 93–96%).

Both, similar total ^{40}Ar concentrations in crushed and fused samples as well as the considerable gas release at high temperatures indicate (i) that the major host phases of trapped argon are fluid or melt inclusions and (ii) a high retentivity of these inclusions, i.e. a significant amount of inclusions decrepitate together with melting of their host minerals.

5. Discussion

Table 3 shows that there is a large spread in individual, sample-specific mantle-$^{40}Ar/^{36}Ar$ compositions (corrected for atmospheric argon that is recognizably associated with atmospheric neon) ranging from 4100, i.e. much lower than observed maximum values of plume-type reservoirs like Loihi, Iceland, or Réunion, respectively (Trieloff et al., 2000; Harrison et al., 2003; Hopp and Trieloff, 2005), up to 39,000, that are typically found in many MORB-samples (Burnard et al., 1997; Moreira et al., 1998; Trieloff et al., 2003). The frequently observed mantle endmember composition with low $^{40}Ar/^{36}Ar$ ratios and relatively high $^{36}Ar/^{22}Ne$ ratios significantly above an estimated oceanic mantle value of 9.2±3.0 (Trieloff et al., 2002) or 8.9±0.6 (Holland and Ballentine, 2006) indicates either (i) admixing of an Ar-rich plume component or (ii) admixing of highly Ar enriched atmospheric fluids. In the following subsections we want to address these two scenarios.

5.1. Model 1: Plume–lithosphere interaction — binary mixing of fractionated mantle components

In Fig. 5 we plotted the mantle-$^{40}Ar/^{36}Ar$ ratios versus the $^{21}Ne/^{22}Ne_{MANTLE}$ values (Table 3) and compare these with other localities and reservoirs

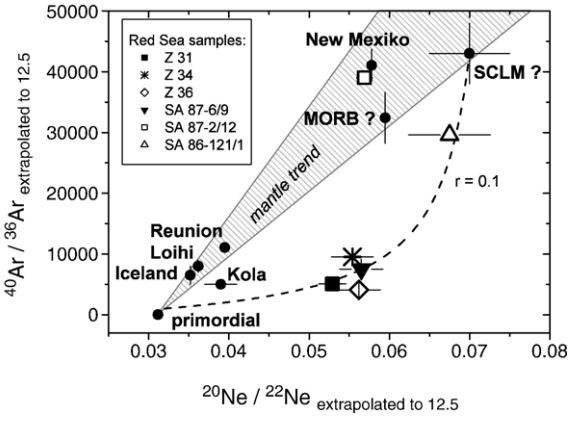

Fig. 5. Mantle argon and neon isotope systematics. Red Sea samples (Z31, Z34, Z36, SA87-6/9#3) plot below a postulated mantle trend that is observed for other locations (filled squares) whereas xenoliths SA 86-121/1 and SA 87-2/12 seem to fit this array more closely. Data from Marty et al. (1998), Harrison et al. (2003), Trieloff and Kunz (2005), Hopp and Trieloff (2005), Holland and Ballentine (2006). Primordial values: $^{40}Ar/^{36}Ar \approx 0$ (solar, e.g. Benkert et al., 1993), $^{21}Ne/^{22}Ne_{Ne-B} = 0.0312 \pm 0.0005$ (Trieloff and Kunz, 2005).

(MORB, Loihi, Iceland, Réunion, Kola, New Mexico) for which estimates of the respective mantle-$^{40}Ar/^{36}Ar$ ratio were reported (Marty et al., 1998; Trieloff et al., 2000; Harrison et al., 2003; Trieloff and Kunz, 2005; Hopp and Trieloff, 2005; Holland and Ballentine, 2006). The OIB and MORB data approximately follow a linear trend, indicated in Fig. 5 as array. The slope of this trend is in accordance with a common radiogenic/nucleogenic evolution with a production ratio of $^{40}Ar^*/^{21}Ne^* = 10^7$ and a mantle-$^{36}Ar/^{22}Ne$ of c. 10, i.e. suggested as unfractionated mantle value. However, most of our results plot significantly below this correlation line.

From He–Ne systematics a hyperbolic mixing trend between a component of lithospheric or asthenospheric provenance and a 'plume' component assigned to the Afar mantle plume source was deduced (Hopp et al., 2004). The authors suggested that melts derived from thermally induced conversion of lithospheric mantle and the asthenosphere mix with plume-related melts. This occurs to a variable degree even on a local scale and could explain observed isotopic variations in He–Ne isotope space. It further requires a relative enrichment of the heavier element Ne versus He in the 'plume' component in respect to the lithospheric/asthenospheric component.

Binary mixing of two in respect to Ar and Ne differently elementally fractionated mantle components would also result in a hyperbolic trajectory in Ar–Ne space (Fig. 5). Such hyperbolic plume-SCLM mixing for both He–Ne and Ne–Ar isotope systematics was also suggested by Buikin et al. (2005) for European subcontinental mantle xenoliths. In a binary mixing model a hyperbolic trend would indicate fractionation between Ar and Ne in one or both mantle endmembers before mixing, characterized by a curvature parameter $r = (^{36}Ar/^{22}Ne)_{SCLM/MORB}/(^{36}Ar/^{22}Ne)_{PLUME}$ of c. 0.1 (Fig. 5). Consequently, either the 'plume' component is enriched in Ar or the lithospheric/asthenospheric component is depleted in Ar relative to each other (or both), i.e. fractionation would again favour a relative enrichment of the heavier element in the 'plume' component. Our results point to the presence of an elevated mantle-$^{36}Ar/^{22}Ne$ ratio relative to unfractionated mantle, i.e.>10. With the implicit assumption that one of both endmembers is unfractionated, these high $^{36}Ar/^{22}Ne$ ratios and the calculated r value of 0.1 would favour a 'plume' component relatively enriched in Ar. Two major fractionation processes could achieve this pattern: solid/melt partitioning and solubility controlled fluid/melt partitioning. Fractionation of Ar and Ne during partial melting (in absence of a free fluid phase, i.e. below saturation depth of CO_2 in melt of c. 30–40 km, Andersen and Neumann, 2001) would require a preferential enrichment of 'plume' Ar in the melt. If we assume the latter suffering smaller degrees of partial melting and hence a larger degree of fractionation between Ar and Ne in the extracted melt, Ar should behave more incompatible than Ne. Though a recent study found no significant difference in partition coefficients $D^{cpx/melt}$ between Ar and Ne (Brooker et al., 2003) this subject is still not fully resolved. Alternatively, separation of a free fluid phase could fractionate Ar and Ne, because the solubilities in silicate melts of both species differ by a factor of c. 3 in favour of Ne (e.g. Jambon et al., 1986; Lux, 1987). In this case, fractionation between Ar and Ne should occur at shallower depth less than c. 30–40 km, after the melt is saturated in CO_2.

It follows that both processes could release a mobile 'plume' related phase – melt or fluid – enriched in Ar relative to Ne and possibly metasomatizing the overlying lithospheric/asthenospheric portion. From Fig. 5 we can conclude that in four samples the proportion between 'plume'- and lithosphere-derived Ar and Ne is very similar. Notably, the only sample for which this model would not apply is SA87-2/12: here we observe a mantle-$^{36}Ar/^{22}Ne$ ratio close to unfractionated mantle and a position on the radiogenic mantle evolution trend in Ar–Ne isotope space (Fig. 5), as it is expected for a MORB type component.

Eventually, degassing processes during magma ascent may further modify the Ar/Ne ratios in the exsolved fluid phases towards higher values.

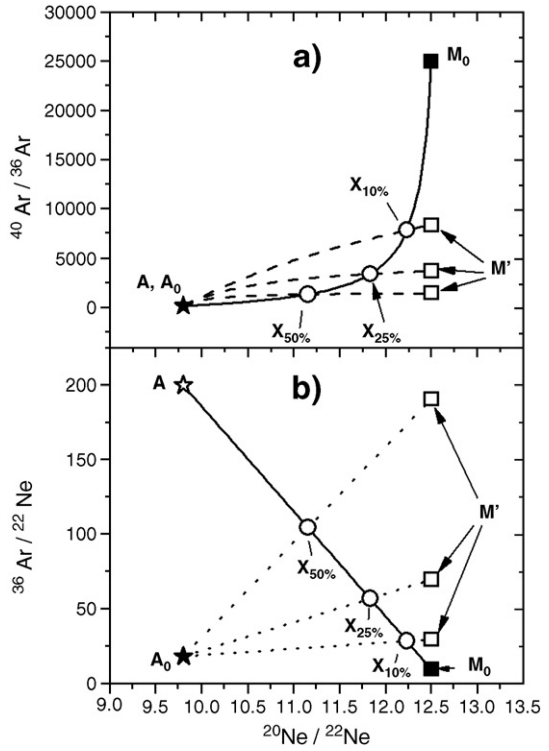

Fig. 6. Isotopic evolution model for a two stage atmospheric contamination process. a) $^{40}Ar/^{36}Ar$ vs. $^{20}Ne/^{22}Ne$ diagram. Shown are primary and secondary mixing hyperbolas, that reflect mixing between initial mantle and a fractionated atmospheric component, and between the resulting mixed component with unfractionated air, respectively. This results in calculation of erroneous mantle-$^{40}Ar/^{36}Ar$ ratios. b) Same for diagram $^{36}Ar/^{22}Ne$ vs. $^{20}Ne/^{22}Ne$. Now mixing is displayed by lines. A, A_0 = fractionated and unfractionated atmosphere; M_0, M′ = initial and apparent mantle; X = mixed composition in the samples, numbers indicate percentage contribution of atmospheric neon. See text for details.

Within this model the rather low mantle-$^{40}Ar/^{36}Ar$ ratios in our Red Sea samples (down to 5040 in sample Z31; 4090 in Z36) imply upper limits for the Ar isotopic composition of the Afar plume component. This is as low as estimated for the Iceland plume source (6000±1500, Trieloff et al., 2000; Harrison et al., 2003; Trieloff and Kunz, 2005) and requires a comparably primitive Afar mantle plume source.

We find, that our observed partly low mantle-$^{40}Ar/^{36}Ar$ ratios could be explained in a simple mixing model between elementally fractionated 'plume' and lithosphere/asthenosphere derived fluids or melts. However, the small variation of our data precludes a clear evidence for the model immanent hyperbolic relationship displayed in Fig. 5.

5.2. Model 2: Admixing of heavily fractionated atmospheric fluids

Atmospheric fluids are characterized by a low $^{40}Ar/^{36}Ar$ ratio of 296. In addition, because of the lower solubility of neon in water relative to argon any interaction of water with mantle-derived rocks can potentially introduce atmospheric fluids with high $^{36}Ar/^{22}Ne$ ratios. E.g. ocean water displays $^{36}Ar/^{22}Ne$ ratios of about 50–70, three times higher than unfractionated air (18.7, Ozima and Podosek, 2002). Many ocean sediments show an even higher argon enrichment with $^{36}Ar/^{22}Ne$ ratios >100 (Staudacher and Allègre, 1988). Mixing of those elementally fractionated fluids with a mantle component (melt or fluid), that is characterized by an unfractionated mantle-$^{36}Ar/^{22}Ne$ ratio of about 10 (Trieloff et al., 2002; Holland and Ballentine, 2006) will inevitably have a much larger impact on the argon isotopic composition compared to neon isotopes.

In Fig. 6a,b we displayed graphically the evolution of a mantle component M_0 with an initial high $^{40}Ar/^{36}Ar$ ratio of 25,000 during interaction with an atmospheric fluid (A) with a $^{36}Ar/^{22}Ne$ ratio of 200, in respect with $^{20}Ne/^{22}Ne$ ratios. Because of the large difference in their $^{36}Ar/^{22}Ne$ ratios admixing of X% atmospheric neon will cause a variation of the $^{40}Ar/^{36}Ar$- and $^{36}Ar/^{22}Ne$ ratios of the resulting hybrid fluid along the shown hyperbola (Fig. 6a)

Table 4
Model results assuming admixing of different fractions Ne (10, 25, 50%) of a fractionated atmospheric component to an unfractionated mantle component

% atm.	$^{20}Ne/^{22}Ne_X$	$^{36}Ar/^{22}Ne_A$	$^{36}Ar/^{22}Ne_X$	r_0	r_X	$r_{M'}$	$^{40}Ar/^{36}Ar_X$	$^{40}Ar/^{36}Ar_{M'}$
10	12.23	50	14	0.2	0.75	0.72	16,177	18,620
25	11.83	50	20	0.2	1.07	1.09	9617	12,432
50	11.15	50	30	0.2	1.60	2.20	4413	6285
10	12.23	200	29	0.05	1.55	1.61	7962	8491
25	11.83	200	57.5	0.05	3.07	3.75	3546	3832
50	11.15	200	105	0.05	5.61	10.21	1472	1587

Two degrees of fractionation are assumed with $^{36}Ar/^{22}Ne$ of fractionated air of 50 and 200, respectively. Other compositions used are: $^{36}Ar/^{22}Ne$ of unfractionated air=18.7; $^{36}Ar/^{22}Ne$ of unfractionated mantle=10; $^{40}Ar/^{36}Ar$ of initial mantle component=25,000. See text for abbreviations and details.

and linear (Fig. 6b) trend, respectively (solid lines). Assuming a rehomogenization between the fluids of both provenances occurred, any later contribution of secondary atmospheric gases (A_0), e.g. by meteoric waters or adsorbed air, would again lead to secondary hyperbolic (Fig. 6a) and linear (Fig. 6b) mixing trends, respectively (dashed lines). Major conclusion from this scenario is, that extrapolated mantle-$^{40}Ar/^{36}Ar$ vs $^{20}Ne/^{22}Ne$ hyperbolic correlations lead to fictitious and lower than initial mantle ratios (M′). As examples we listed results for several used parameters in Table 4. Contribution of a primary atmospheric component with 10%, 25% and 50% atmospheric neon is modeled for two elementally fractionated atmospheric fluids having a $^{36}Ar/^{22}Ne$ ratio of 50 and 200. Initial mantle-$^{40}Ar/^{36}Ar$- and $^{36}Ar/^{22}Ne$ ratios are 25,000 and 10, respectively.

Within such a scenario, the low $^{40}Ar/^{36}Ar$ ratios of samples Z31#1, Z34#1, Z36#1 and SA87-6/9#3 would be caused by an Ar-rich atmospheric contaminant, with the original mantle endmember having an extrapolated $^{21}Ne/^{22}Ne$ of 0.055 and $^{40}Ar/^{36}Ar$ within the grey shaded area in Fig. 5, between c. 25,000 and 40,000. This mantle endmember would be a (linear) mixture of plume type neon and argon and SCLM type neon ($^{21}Ne/^{22}Ne=0.07$) and argon ($^{40}Ar/^{36}Ar=40{,}000–60{,}000$).

5.3. Possible origins of atmospheric contributions

In the last section we discussed a two stage contamination of a mantle component with atmospheric noble gases. In the second stage we generally observe a late surface-related addition of air, introduced e.g. by adsorption, alteration phases, laboratory treatment, or other contamination mechanisms possibly related to magma chamber processes. This secondary atmospheric component is released separately during the extraction process, either by crushing or by heating. In contrast, we postulate a common extraction of a primary atmospheric component together with intrinsic mantle noble gases. This could be caused either by a similar degassing behaviour of distinct fluid inclusion assemblages of atmospheric and mantle provenance during the extraction process or by a physical homogenization of both fluid components before final entrapment into the recovered ultramafic rocks.

Up to now, because of their small sizes with exception of sample Z31 no microthermometry of the fluid inclusions has been performed. For Z31, Kurat et al. (1993) reported the existence of partly biphased CO_2-inclusions with minimum pressures of 0.3 GPa, indicating a deeper level of entrapment, and inclusions containing halite and carbonates, for which no *P–T* conditions were mentioned.

We demand that any primary atmospheric component present in samples of the SCLM should be characterized by elementally fractionated high $^{36}Ar/^{22}Ne$ ratios as compared to unfractionated air (= c. 19). This type of fractionation is quite common in rocks that interacted with hydrous fluids, e.g. oceanic crust (Staudacher and Allègre, 1988), because Ar is better soluble in water than Ne. A relative late and shallow homogenization process between mantle fluids and percolating water in a magma column predating the trapping event would favour rather shallow trapping conditions. A contribution of fluids inherent to the deeper crust appears rather unlikely because due to the much higher concentrations of K, U, and Th in the continental crust, such fluids generally show high amounts of radiogenic (^4He, ^{40}Ar) or nucleogenic (^{21}Ne) isotopes (e.g. Kennedy et al., 1990; Hiyagon and Kennedy, 1992; Drescher et al., 1998), which is not reflected by our data.

Several recent studies postulated a subduction-related contribution of atmospheric noble gases, in particular argon, to the mantle source of continental ultramafics (Matsumoto et al., 2001; Yamamoto et al., 2004) or MORB (Sarda et al., 1999; Sarda, 2004). These interpretations base strongly on low $^{40}Ar/^{36}Ar$ ratios, suggesting atmospheric contributions. If model 2 applies, the primary contamination with atmospheric noble gases might be derived from a dehydrating subducting slab, opening a perspective for future tracing of slab derived fluids. However, the last subduction event in the Red Sea area took place during the Pan African, i.e. c. 600–800 Ma ago. Therefore, we also have to account for slab-immanent *in-situ* radiogenic production of $^{40}Ar^*$ and $^4He^*$ (atmospheric He is negligible). The relative contributions of radiogenic, atmospheric, and mantle noble gases highly depend on model assumptions about K, U, and Th concentrations in the lithospheric mantle and in the slab, and the absolute amount of mantle and relict trapped atmospheric noble gases. We may assume as boundary condition that the time integrated composition of the atmosphere-type subduction related fluid should not exceed a $^{40}Ar/^{36}Ar=1000$ to warrant the model assumptions discussed above. A simple calculation taking 800 Ma and today atmospheric composition as initial conditions requires a $K/^{36}Ar$ ratio in the slab component of 10^8. Provided the increase in K concentration in the respective influenced lithospheric mantle portion is between 1 and 100 ppm, the associated input of slab derived ^{36}Ar leads to a concentration rise in the SCLM of about $5\cdot10^{-12}$ to $5\cdot10^{-10}$ ccm STP $^{36}Ar/g$. In an independent approach Holland and Ballentine (2006) calculated a seawater derived ^{36}Ar concentration in the convecting mantle of about $6\cdot10^{-11}$ ccm STP/g. Though

these estimates of course depend on the age of the slab and may vary for the convecting and shallow mantle, necessary ^{36}Ar and K concentrations appear to be reasonable.

Similar suggestions for helium had been done previously by Dunai and Baur (1995). They proposed that a 1–2% contribution of 300 Ma old subducted crust within the mantle source of European xenoliths is enough to account for the observed more radiogenic ^{3}He/^{4}He ratios relative to MORB values. Hence, the isotopic pattern of He and Ar allows a significant subduction-related influence on mantle noble gas signatures.

6. Summary and conclusions

Observed ^{40}Ar/^{36}Ar ratios of mantle-derived rocks of the subcontinental lithospheric mantle (SCLM) from the Red Sea region encompass sample-specific maximum ratios from c. 4190±100 to 25,590±620 (sample SA87-2/12), the latter being the highest value of any mantle xenolith sample observed so far (except for diamonds, Wada and Matsuda, 1998). Mixing correlations between atmosphere and mantle-derived argon and neon were used to calculate respective mantle-^{40}Ar/^{36}Ar ratios at ^{20}Ne/^{22}Ne=12.5. We obtained mantle-^{40}Ar/^{36}Ar ratios of 5040±50, 7500±70, 9510±220, 29,600±2700 and 39,000±2500 (samples Z31, SA87-6/9, Z34, SA 86-121/1 and SA 87-2/12, respectively). These results and the large range of observed sample-specific maximum ratios point to a heterogeneous argon composition of the Red Sea SCLM. Two scenarios were addressed:

(i) In a simple 'plume'−lithosphere binary mixing scenario this requires a low ^{40}Ar/^{36}Ar (i.e. <4000) composition of the 'plume' derived argon and a ^{36}Ar/^{22}Ne ratio representing the subcontinental lithospheric mantle that is lower than the corresponding value of the 'plume' source. The observed elevated mantle-^{36}Ar/^{22}Ne ratios (i.e. higher than unfractionated mantle-^{36}Ar/^{22}Ne ratio of c. 10, Trieloff et al., 2002; Trieloff and Kunz, 2005; Holland and Ballentine, 2006) demands for a substantial degree of elemental fractionation of the 'plume' component either caused by partial melting or melt/fluid separation processes. Subsequently these fractionated fluids would metasomatize the overlying lithospheric/asthenospheric mantle portion.

(ii) In an alternative model, a two stage contamination scenario with atmospheric fluids is proposed. The first stage contaminant should be heavily elementally fractionated displaying elevated ^{36}Ar/^{22}Ne ratios relative to unfractionated air. This kind of fractionation is a common feature of phases in contact with water (oceanic crust, deep-sea sediments, alteration products). After mixing with mantle Ar and Ne, a subsequent late-stage contribution of atmospheric gases at or close to the surface will produce the observed correlation pattern in Ar–Ne isotope space, that yield fictitious and low mantle-^{40}Ar/^{36}Ar ratios. Because of the elevated Ar/Ne ratio of the first atmospheric contaminant this will hardly affect the Ne isotopic composition. Two different source regions for the proposed primary atmospheric fluids could be envisaged: a shallow introduction of hydrous fluids into the rising magma column or a deeper contribution of remobilized subducted atmospheric noble gases. As required, both realms of fluids would be characterized by elevated ^{36}Ar/^{22}Ne ratios. A simple calculation for a lithosphere age of 800 Ma and with a common range in K- and ^{36}Ar-concentrations shows that it is possible to keep an atmospheric argon component sufficiently unaffected from radiogenic ingrowth of ^{40}Ar*.

Acknowledgements

The authors cordially thank E. Burkert, H. Richter and H. Funke for their technical assistance and J. Kiko and T. Kirsten for their support. Gero Kurat kindly provided the samples. Extraordinarily detailed comments by two anonymous reviewers considerably improved this manuscript. JH and MT acknowledge funding by the Deutsche Forschungsgemeinschaft.

Appendix A. Supplementary data

Supplementary data associated with this article can be found, in the online version, at doi:10.1016/j.chemgeo.2007.01.004.

References

Albarède, F., 1998. Time-dependent models of U–Th–He and K–Ar evolution and the layering of mantle convection. Chem. Geol. 145, 413–429.

Allègre, C.J., Hofmann, A.W., O'Nions, R.K., 1996. The argon constraints on mantle structure. Geophys. Res. Lett. 23, 3555–3557.

Altherr, R., Henjes-Kunst, F., Baumann, A., 1990. Asthenosphere versus lithosphere as possible sources for basaltic magmas erupted during formation of the Red Sea: constraints from Sr, Pb and Nd isotopes. Earth Planet. Sci. Lett. 96, 269–286.

Andersen, T., Neumann, E.-R., 2001. Fluid inclusions in mantle xenoliths. Lithos 55, 301–320.

Ballentine, C.J., Barfod, D.N., 2000. The origin of air-like noble gases in MORB and OIB. Earth Planet. Sci. Lett. 180, 39–48.

Ballentine, C.J., Marty, B., Sherwood Lollar, B., Cassidy, M., 2005. Neon isotopes constrain convection and volatile origin in the Earth's mantle. Nature 433, 33–38.

Barfod, D.N., Ballentine, C.J., Halliday, A.N., Fitton, J.G., 1999. Noble gases in the Cameroon line and the He, Ne, and Ar isotopic compositions of high μ (HIMU) mantle. J. Geophys. Res. 104, 29,509–29,527.

Benkert, J.P., Baur, H., Signer, P., Wieler, R., 1993. He, Ne, and Ar from the solar wind and solar energetic particles in lunar ilmenites and pyroxenes. J. Geophys. Res. 98, 13147–13162.

Bosch, D., Bruguier, O., 1998. An early Miocene age for a high temperature event in gneisses from Zabargad Island (Red Sea, Egypt): mantle diapirism? Terra Nova 10, 274–279.

Brandstaetter, F., Ntaflos, T., Kurat, G., 1993. Electron microprobe analyses of minerals from peridotites and associated vein rocks of Zabargad Island, Red Sea, Egypt. Special Publication Mineralogisch-Petrographische Abteilung. Naturhistorisches Museum, Vienna.

Brooker, R.A., Du, Z., Blundy, J.D., Kelley, S.P., Allan, N.L., Wood, B.J., Chamorro, E.M., Wartho, J.-A., Purton, J.A., 2003. The 'zero charge' partitioning behaviour of noble gases during mantle melting. Nature 423, 738–741.

Brueckner, H.K., Zindler, A., Seyler, M., Bonatti, E., 1988. Zabargad and the isotopic evolution of the sub-Red Sea mantle and crust. Tectonophysics 150, 163–176.

Brueckner, H.K., Elhaddad, M.A., Hamelin, B., Hemming, S., Kröner, A., Reisberg, L., Seyler, M., 1995. A Pan African origin and uplift for the Gneisses and peridotites of Zabargad Island, Red Sea: A Nd, Sr, Pb, and Os isotope study. J. Geophys. Res. 100, 22,283–22,297.

Buikin, A., Trieloff, M., Hopp, J., Althaus, T., Korochantseva, E., Schwarz, W.H., Altherr, R., 2005. Noble gas isotopes suggest deep mantle plume source of late Cenozoic mafic alkaline volcanism in Europe. Earth Planet. Sci. Lett. 230, 143–162.

Burnard, P., Graham, D., Turner, G., 1997. Vesicle-specific noble gas analyses of "popping rock": implications for primordial noble gases in Earth. Science 276, 568–571.

Drescher, J., Kirsten, T., Schäfer, K., 1998. The rare gas inventory of the continental crust, recovered by the KTB Continental Deep Driling Project. Earth Planet. Sci. Lett. 154, 247–263.

Dunai, T., Baur, H., 1995. Helium, neon, and argon systematics of the European subcontinental mantle: implications for its geochemical evolution. Geochim. Cosmochim. Acta 59, 2767–2783.

Fuhrmann, U., Lippolt, H.J., Hess, J., 1987. Examination of some proposed K–Ar standards: $^{40}Ar/^{39}Ar$ analyses and conventional K–Ar data. Chem. Geol., Isot. Geosci. Sect. 66, 41–51.

Harrison, D., Burnard, P., Trieloff, M., Turner, G., 2003. Resolving atmospheric contaminants in mantle noble gas analyses. Geochem. Geophys. Geosyst. 4 (3) (2002GC000325).

Henjes-Kunst, F., Altherr, R., Baumann, A., 1990. Evolution and composition of the lithospheric mantle underneath the western Arabian Peninsula: constraints from Sr–Nd isotope systematics of mantle xenoliths. Contrib. Mineral. Petrol. 105, 460–472.

Hiyagon, H., Kennedy, B.M., 1992. Noble gases in CH_4-rich gas fields, Alberta, Canada. Geochim. Cosmochim. Acta 56, 1569–1589.

Holland, G., Ballentine, C.J., 2006. Seawater subduction controls the heavy noble gas composition of the mantle. Nature 441, 186–191.

Hopp, J., Trieloff, M., 2005. Refining the noble gas record of the Réunion mantle plume source: implications on mantle geochemistry. Earth Planet. Sci. Lett. 240, 573–588.

Hopp, J., Trieloff, M., Altherr, R., 2004. Neon isotopes in mantle rocks from the Red Sea region reveal large-scale plume–lithosphere interaction. Earth Planet. Sci. Lett. 219, 61–76.

Jambon, A., Weber, H.W., Begemann, F., 1985. Helium and argon from an Atlantic MORB glass: concentration, distribution and isotopic composition. Earth Planet. Sci. Lett. 73, 255–267.

Jambon, A., Weber, H., Braun, O., 1986. Solubility of He, Ne, Ar, Kr, and Xe in a basalt melt in the range 1250°–1600 °C, geochemical implications. Geochim. Cosmochim. Acta 50, 401–408.

Kennedy, B.M., Hiyagon, H., Reynolds, J.H., 1990. Crustal neon: a striking uniformity. Earth Planet. Sci. Lett. 98, 277–286.

Kurat, G., Palme, H., Embey-Isztin, A., Touret, J., Ntaflos, T., Spettel, B., Brandstätter, F., Palme, C., Dreibus, G., Prinz, M., 1993. Petrology and geochemistry of peridotites and associated vein rocks of Zabargad Island, Red Sea, Egypt. Mineral. Petrol. 48, 309–341.

Langmuir, C.H., Vocke Jr., R.D., Hanson, G.N., Hart, S.R., 1978. A general mixing equation with applications to Icelandic basalts. Earth Planet. Sci. Lett. 37, 380–392.

Lanphere, M.A., Dalrymple, G.B., 1976. Identification of excess Argon by the ^{40}Ar–^{39}Ar age spectrum technique. Earth Planet. Sci. Lett. 32, 141–148.

Lux, G., 1987. The behaviour of noble gases in silicate liquids: solution, diffusion, bubbles and surface effects, with applications to natural samples. Geochim. Cosmochim. Acta 51, 1549–1560.

Marty, B., Humbert, F., 1997. Nitrogen and argon isotopes in oceanic basalts. Earth Planet. Sci. Lett. 152, 101–112.

Marty, B., Pik, R., Gezahegn, Y., 1996. Helium isotopic variations in Ethiopian plume lavas: nature of magmatic sources and limit on lower mantle contribution. Earth Planet. Sci. Lett. 144, 223–237.

Marty, B., Tolstikhin, I., Kamensky, I.L., Nivin, V., Balaganskaya, E., Zimmermann, J.-L., 1998. Plume-derived rare gases in 380 Ma carbonatites from the Kola region (Russia) and the argon isotopic composition in the deep mantle. Earth Planet. Sci. Lett. 164, 179–192.

Matsumoto, T., Honda, M., McDougall, I., O'Reilly, S.Y., Norman, M., Yaxley, G., 2000. Noble gases in pyroxenites and metasomatised peridotites from the Newer Volcanics, southeastern Australia: implications for mantle metasomatism. Chem. Geol. 168, 49–73.

Matsumoto, T., Chen, Y., Matsuda, J., 2001. Concomitant occurrence of primordial and recycled noble gases in the Earth's mantle. Earth Planet. Sci. Lett. 185, 35–47.

Moreira, M., Kunz, J., Allègre, C.J., 1998. Rare gas systematics in popping rock: Isotopic and elemental compositions in the upper mantle. Science 279, 1178–1181.

Nicolas, A., Boudier, F., 1987. Structure of Zabargad Island and early rifting of the Red Sea. J. Geophys. Res. 92, 461–474.

Ozima, M., Podosek, F.A., 2002. Noble Gas Geochemistry, 2nd ed. Cambridge University press, Cambridge. 286 pp.

Sarda, P., 2004. Surface noble gas recycling to the terrestrial mantle. Earth Planet. Sci. Lett. 228, 49–63.

Sarda, P., Moreira, M., Staudacher, T., 1999. Argon–lead isotopic correlation in mid-Atlantic ridge basalts. Science 283, 666–668.

Scarsi, P., Craig, H., 1996. Helium isotope ratios in Ethiopian Rift basalts. Earth Planet. Sci. Lett. 144, 505–516.

Schaeffer, G.A., Schaeffer, O.A., 1977. ^{40}Ar–^{39}Ar ages of lunar rocks. Proc. Lun. Plan. Sci. Conf. 8th, pp. 2253–2300.

Staudacher, T., Allègre, C.J., 1988. Recycling of oceanic crust and sediments: the noble gas subduction barrier. Earth Planet. Sci. Lett. 89, 173–183.

Staudacher, T., Sarda, P., Richardson, S.H., Allègre, C.J., Sagna, I., Dmitriev, L.V., 1989. Noble gases in basalt glasses from a Mid-Atlantic Ridge topographic high at 14°N: geodynamic consequences. Earth Planet. Sci. Lett. 96, 119–133.

Steiger, R.H., Jäger, E., 1977. Subcommision on geochronology: convention on the use of decay constants in geo- and cosmochronology. Earth Planet. Sci. Lett. 36, 359–362.

Trieloff, M., Kunz, J., 2005. Isotope systematics of noble gases in the Earth's mantle: possible sources of primordial isotopes and implications for mantle structure. Phys. Earth Planet. Inter. 148, 13–38.

Trieloff, M., Weber, H.W., Kurat, G., Jessberger, E.K., Janicke, J., 1997. Noble gases, their carrier phases, and argon chronology of upper mantle rocks from Zabargad Island, Red Sea. Geochim. Cosmochim. Acta 61, 5065–5088.

Trieloff, M., Kunz, J., Clague, D.A., Harrison, D., Allègre, C.J., 2000. The nature of pristine noble gases in mantle plumes. Science 288, 1036–1038.

Trieloff, M., Kunz, J., Allègre, C.J., 2002. Noble gas systematics of the Réunion mantle plume source and the origin of primordial noble gases in Earth's mantle. Earth Planet. Sci. Lett. 200, 297–313.

Trieloff, M., Falter, M., Jessberger, E.K., 2003. The distribution of mantle and atmospheric argon in oceanic basalt glasses. Geochim. Cosmochim. Acta 67, 1229–1245.

Volker, F., McCulloch, M.T., Altherr, R., 1993. Submarine basalts from the Red Sea: new Pb, Sr, and Nd isotopic data. Geophys. Res. Lett. 20, 927–930.

Volker, F., Altherr, R., Jochum, K.-P., McCulloch, M.T., 1997. Quaternary volcanic activity of the southern Red Sea: new data and assessment of models on magma sources and Afar plume–lithosphere interaction. Tectonophysics 278, 15–29.

Wada, N., Matsuda, J., 1998. A noble gas study of cubic diamonds from Zaire: constraints on their mantle source. Geochim. Cosmochim. Acta 62, 2335–2345.

Yamamoto, J., Kaneoka, I., Nakai, S., Kagi, H., Prikhod'ko, V.S., Arai, S., 2004. Evidence for subduction-related components in the subcontinental mantle from low $^{3}He/^{4}He$ and $^{40}Ar/^{36}Ar$ ratio in mantle xenoliths from Far Eastern Russia. Chem. Geol. 207, 237–259.